Electronic properties of rutile and anatase TiO_2 and their effect on CO_2 adsorption: a comparison of first principle approaches

Žan Kovačič[1], Blaž Likozar*[1], Matej Huš*[1,2,3]

[1] National Institute of Chemistry, Department of Catalysis and Chemical Reaction Engineering, Hajdrihova 19, SI-1000 Ljubljana, Slovenia

[2] Association for Technical Culture (ZOTKS), Zaloška 65, SI-1000 Ljubljana, Slovenia

[3] University of Nova Gorica, Vipavska 13, SI-5000 Nova Gorica, Slovenia

*Corresponding authors: blaz.likozar@ki.si, matej.hus@ki.si

Abstract

Photocatalysis is a promising technique for utilizing solar light in chemical synthesis. Among several effective photocatalysts, TiO_2 remains the archetypal representative. Using density functional theory calculations, we characterized the geometric, mechanical, electronic and optical properties of rutile and anatase TiO_2. We show that a proper choice of the functional and corrections is of paramount importance. While the geometric and mechanical properties are well reproduced with conventional GGA functionals, electronic properties require at least a Hubbard approach. Despite being revered as superior, hybrid functionals do not necessarily perform better and a prudent choice is required. On the contrary, a lower Hubbard correction is desirable for a proper description of interactions, defects and structures. Lastly, CO_2 adsorption was studied on several surfaces. Pristine anatase and rutile surfaces poorly activate CO_2, with the exception of rutile (001), which binds CO_2 strongly in a bent form, showing considerable charge transfer and activation.

Keywords: Density Functional Theory (DFT), DFT+U, hybrid functionals, TiO_2, CO_2 adsorption

1. Introduction

Titanium dioxide (TiO_2) has received significant attention recently due to its wide range of applications. Although useful in catalysis, coating industry or as antibacterial agent [1], it stands out for photocatalytic properties. Appearing in different crystal phases, the most common phases of TiO_2 in nature are rutile, anatase and brookite [2], whilst other polymorphs such as cotunnite-type, abaddeleyite-type, pyrite-type, columbite-type have also been discovered [3]. In photocatalysis, the most studied polymorphs are anatase and rutile thanks to their superior photoactivity, while brookite is only occasionally included.

One of the crucial characteristics of photocatalytic materials is the band gap, which corresponds to the energy required to excite an electron from the valence band to the conduction band, yielding excited electrons required for photoreductive reactions. The drawback of using pure TiO_2 is its large band gap (anatase: 3.2 eV; rutile: 3.0 eV), limiting its activity to the UV. This allows to exploit only 4 % of the incident solar light, while the visible light accounts for roughly another 43 % of the solar energy [4].

Several contingencies are available to increase the photocatalytic activity of TiO_2. Doping (e.g. N [5], S [6], C [7]) can decrease the band gap but caution should be taken as doping can also introduce mid-gap states, which act as recombination centers and hinder the activity [8]. Co-doping (e.g. N or C, Nb or Ta [9], C, N, S [10]), can be used to avoid this problem [9]. Another approach to improve the photocatalytic activity is the deposition of a co-catalyst on the surface. These are usually (noble) metals (e.g. Au [11], Ag [12], Ni, Cu, Co [13], Cr, Fe [14], Pt [15]), which act as electron traps and promote charge separation [16, 17]. Surface defects (e.g. oxygen vacancies) exhibit similar tendencies [18], whereas bulk defects act as recombination centers [19]. Another option is to combine different semiconductors into the so-called Z-scheme photocatalysts (e.g. Ag_3PO_4/TiO_2 [20], g-

C_3N_4/TiO_2 [21], TiO_2/NiS [22]), which exploit a high conduction band minimum of one semiconductor and a low valence band maximum of the other.

As described, there are a plethora of possibilities for tuning of photocatalysts. As experimental probing of all possible modifications and their combinations has proved time- and resource-consuming, computer simulations have become a more popular surrogate. Recent advances in available computational power and theoretical techniques have made it possible to rely increasingly on *in silico* results. However, the choice of the method used is paramount for obtaining meaningful results. For instance, in density functional theory, the choice of the exchange functional has profound effects on the outcome. While LDA and GGA produce reasonable geometries, they fail to correctly predict the electronic properties of TiO_2 [23]. A cheap way to rectify this problem is by applying a Hubbard correction (DFT+U) [24] on localized *d* and *f* electrons, which effectively adds a screened Coulomb interaction [25]. While it is computationally not more expensive, the drawback of the method is that U has to be chosen arbitrarily to reproduce the desired property and is in general not transferrable between different materials [26]. Hybrid functionals *can* yield superior agreement with experiments at the expense of the computational cost, provided that an appropriate functional is chosen.

Climate change has prompted scientists to search for ways to reduce the emissions or otherwise utilize CO_2, preferably converting it into value-added products. One of the most promising approaches is photocatalytic CO_2 conversion, where TiO_2 has received extensive attention due to its proven record in the field. Although pristine TiO_2 surfaces exhibit poor photoactivity, incorporation of surface defects such as oxygen vacancies [27], doping [28], deposition of co-catalysts [29] or Z-scheme [30] catalysts have proven to substantially increase their activity due to improved charge separation, increased charge transfer and lower band gap [31, 32]. Nevertheless, photoactivity of the catalyst is not sufficient as the catalyst must also bind the reactants strongly enough. As it will be shown later on, we studied how different TiO_2 structures and surfaces bind and activate CO_2.

In photocatalysis, anatase and rutile are predominantly used. While rutile is the more stable phase under ambient conditions, anatase is more active. It is believed that the larger band gap of anatase increases the oxidation strength of photoexcited electrons [33], which promotes the activity. The charge carrier lifetime is also generally longer in indirect band gap semiconductors (anatase) than in direct ones (rutile) [34], usually an order of magnitude. As found by Luttrell et al. [35] charge carriers can originate from much deeper in the bulk for anatase as opposed to rutile, increasing the activity. Zhang et al. have shown [36] that the average effective mass of photogenerated charge carriers (holes and electrons), which has a profound effect on their migration rate and recombination. They calculated that the average effective mass for electrons and holes was smaller in anatase compared to rutile. This facilitates their migration, prevents recombination and in turn boosts the photocatalytic activity [37]. It is also important to note that different surfaces exhibit different activities, as well as band gaps, demonstrated by Pan et al. [38]. The catalyst characteristics differ not only among different materials but also among different surfaces of the same material.

In this work, we studied and compared the geometric, mechanical and electronic properties of rutile and anatase crystal phases of TiO_2. They were compared using different types of functionals and corrections (PBE, PBE+U (*U*-*J*=4, 6 and 8 eV), PBE+U+D3 and hybrid functionals PBE0, B3LYP and HSE06) within the density functional theory framework. We demonstrated that choosing a proper functional is of crucial importance for a proper description. Furthermore optical properties were investigated. Finally, we examined three most common anatase and rutile surfaces for adsorption and subsequent activation of CO_2. We show that rutile (001) is the only active TiO_2 surface for CO_2 activation among the tested ones. Moreover, we show that HSE06 yields a superior description of the electronic properties of TiO_2. When the computational cost is prohibitive, a proper Hubbard correction to GGA functionals is also acceptable. B3LYP and PBE0 performed worse, thus not justifying their computational cost.

2. Theoretical methods

The calculations were performed in GPAW 20.1.0 [39] with the projector augmented wave method (PAW) as implemented in the plane-wave approach. Fermi-Dirac smearing of 0.01 eV was applied. Spin-polarized calculations were not necessary as the magnetic moments were shown to be quenched. The Hubbard [24] term was employed to take into account the strong on-site Coulomb interactions of localized electrons. We follow the approach by Dudarev [40], where a single value of *U-J* (non-normalized) is used (in our case 4, 6 and 8 eV) on Ti 3*d* orbitals, since O and C lack occupied *d* orbitals. Long range dispersion forces were accounted for through the Grimme-D3 [41] correction.

The energy cut off for the wave function was set at 500 eV as determined by convergence tests. The unit cells of rutile and anatase TiO_2 were sampled with a Monkhorst-Pack mesh [42] using 16x16x16 and 16x16x8 k-points, respectively. Due to the size of surface slab supercells, a 2x2x1 k-point mesh sufficed. To avoid spurious interactions between the periodic slabs, a 12 Å vacuum in the *z*-direction with a dipole correction [43] was employed.

For surface slabs, 2x2 supercells were used (except for rutile (110) surface where a 3x2 supercell was required). The bulk modulus was calculated as a second derivative of energy with respect to the unit cell volume (unit cell was varied from 95 to 105 % of the most stable size with increment of 1 %), and then fit with the stabilized jellium equation of state (SJEOS) [44]. The dielectric function (constant) was calculated with the linear dielectric response of an extended system as implemented in GPAW within the random phase approximation (RPA) [43, 44]. The parameter *nbands* was set at quadruple the number of occupied bands, *ecut* for local field effect at 40 eV and the broadening parameter *eta* at 0.05 eV. The scissoring operator [47] was applied (unless otherwise specified) to correct for the incorrect band gap predictions by the functionals. The (absolute) scissoring value was obtained as the difference between the calculated and the experimentally determined band gap.

For CO_2 adsorption, all possible adsorption sites were considered. The adsorption energies were calculated as:

$$\Delta E_{ads} = E_{species+slab} - E_{slab} - E_{species} \quad (1)$$

where $E_{species+slab}$ is the energy of the slab with the adsorbate, E_{slab} is the energy of the empty slab and $E_{species}$ is the energy of the relaxed adsorbate in the gaseous phase.

The effective mass of photogenerated charge carriers (holes and electrons) was calculated as $m^* = \hbar^2 \left(\frac{\mathrm{d}^2 E}{\mathrm{d}k^2}\right)^{-1}$,

where $\hbar$ is the reduced Planck constant, *E* is the electronic energy and *k* is the wave vector of the band.

3. Results and discussion

3.1 Geometry and mechanical properties

While different functionals and approaches generally struggle least with the prediction of geometries, they represent a useful starting point to dismiss the obviously ill-suited approaches. Throughout this work, we compare the plain PBE approach, the effects of Grimme's D3 correction, three different Hubbard values applied on top of PBE (U - J = 4, 6, 8 eV) and three most common hybrid functionals (PBE0, HSE06, B3LYP). Henceforth, we label the approaches as: PBE, PBE+4, PBE+6, PBE+8, PBE+4+D3, PBE+6+D3, PBE+8+D3, HSE06, PBE0 and B3LYP.

In this section, we focus our attention to the performance of the functionals in describing the geometry and mechanical properties. First, bulk crystal structures of rutile and anatase were optimized at different levels of theory and compared with experimental values from the literature. The results are summarized in Table 1.

Table 1: Optimized structural parameters, bulk modulus, and equilibrium volume for rutile TiO_2

	a=b [Å]	c [Å]	B [GPa]	V0 [Å^3]
experimental	4.586 [48]	2.954	216.0	62.13
PBE	4.657 (+1.55 %)	2.990 (+1.22 %)	226.4 (+4.81 %)	64.49 (+3.80 %)
PBE+4	4.666 (+1.74 %)	3.014 (+2.03 %)	220.3 (+1.99 %)	65.29 (+5.09 %)
PBE+6	4.670 (+1.83 %)	2.999 (+1.52 %)	225.0 (+4.17 %)	65.78 (+5.87 %)
PBE+8	4.676 (+1.96 %)	3.031 (+2.61 %)	227.3 (+5.23 %)	66.19 (+6.53 %)
PBE+4+D3	4.649 (+1.37 %)	2.995 (+1.39 %)	231.7 (+7.27 %)	64.62 (+4.00 %)

PBE+6+D3	4.653 (+1.46 %)	3.010 (+1.90 %)	232.4 (+7.59 %)	65.08 (+4.75 %)
PBE+8+D3	4.659 (+1.59 %)	3.023 (+2.34 %)	233.1 (+7.92 %)	65.52 (+5.46 %)
HSE06	4.593 (+0.15 %)	2.951 (-0.10 %)	260.1 (+20.42 %)	62.16 (+0.05 %)
PBE0	4.601 (+0.33 %)	2.951 (-0.10 %)	262.6 (+21.57 %)	62.12 (-0.02 %)
B3LYP	4.652 (+1.44 %)	2.958 (+0.14 %)	241.4 (+11.76 %)	63.86 (+2.78 %)

The experimentally determined lattice constants for rutile TiO_2 are a = 4.586 Å and c = 2.954 Å [48]. The PBE functional yields similar values of 4.657 Å (+1.55 %) and 2.990 Å (+1.22 %), respectively. Applying the Hubbard parameter causes slight underbinding and increases the unit cell. The Hubbard correction of 4 eV increases the lattice constants by 1.74 % and 2.03 %, whereas for 8 eV the increase is 1.96 % and 2.61 % for a and c, respectively. Similar effects have been previously observed in the literature, where the increase of U-J was shown to generally elongate the lattice [40]. Conversely, including the Grimme D3 dispersion corrections causes stronger binding, leading to a smaller overshoot of the unit cell parameters. The hybrid functionals HSE06 and PBE0 output similar results, which are very close to experimental lattices (less than 0.33 %), whereas B3LYP elongates the a cell parameter (+1.44 %) but not c (+0.14 %).

The optimized structures were subsequently used as input to obtain the bulk modulus (see Table 1). The unit cell was varied from 95 to 105 % (with a 1 % increment) size of the optimized structure. The calculated volumes and energies were then fit by the stabilized jellium equation of state (SJEOS) [44]. Interestingly, the experimental value of bulk modulus for rutile (216 GPa) [49] is closely reproduced by the PBE functional (226.4 GPa). Applying the Hubbard parameter further improves the predictions (for 4 eV it comes even closer to 220.3 GPa) (within 2 %). Further increase of the Hubbard parameter increases the bulk modulus slightly. Adding the Grimme D3 correction increases the bulk modulus further, which could be due to the stronger binding of the structure. All hybrid functionals overestimate the bulk modulus quite significantly (in the range of 10-20 %). Other reported values in literature are 209 GPa (LDA) [2] , 240 GPa (LDA) [50], 235 GPa (PBE) [51] 242 GPa and 253 GPa (LDA)

[52]. This shows that a more sophisticated method does not necessarily translate into better bulk modulus predictions if it has not been optimised for the calculation of that property.

Table 2: Optimized structural parameters, bulk modulus, and equilibrium volume for anatase TiO_2

	a [Å]	c [Å]	B [GPa]	V0 [Å^3]
experimental	3.782 [48]	9.502	179.0 [49]	135.91
PBE	3.815 (+0.87 %)	9.691 (+1.99 %)	205.7 (+14.92 %)	141.04 (+3.77 %)
PBE+4	3.844 (+1.64 %)	9.689 (+1.97 %)	207.4 (+15.87 %)	143.27 (+5.42 %)
PBE+6	3.857 (+1.98 %)	9.669 (+1.76 %)	208.1 (+16.26 %)	144.30 (+6.17 %)
PBE+8	3.872 (+2.34 %)	9.680 (+1.87 %)	208.6 (+16.54 %)	145.45 (+7.02 %)
PBE+4+D3	3.839 (+1.51 %)	9.644 (+1.49 %)	211.6 (+18.21 %)	141.45 (+4.08 %)
PBE+6+D3	3.851 (+1.82 %)	9.611 (+1.15 %)	212.5 (+18.72 %)	142.49 (+4.84 %)
PBE+8+D3	3.860 (+2.06 %)	9.626 (+1.30 %)	213.1 (+19.05 %)	143.64 (+5.69 %)
HSE06	3.772 (-0.26 %)	9.595 (+0.98 %)	237.5 (+32.68 %)	136.23 (+0.24 %)
PBE0	3.774 (-0.21 %)	9.625 (+1.29 %)	238.9 (+33.46 %)	136.03 (+0.09 %)
B3LYP	3.791 (+0.24 %)	9.721 (+2.30 %)	222.3 (+24.19 %)	139.47 (+2.62 %)

Similar trends are observed for anatase, which has experimentally measured lattice constants of a = 3.782 and c = 9.502 Å [48]. As shown in Table 2, PBE predicts unit cell constants of 3.815 Å (+0.87 %) and 9.691 Å (1.99 %) for a and c, respectively. Again, the Hubbard correction seems to slightly underbind the structure, yet the unit cell expansion is caused solely by the elongation of the a parameter. The Grimme D3 correction binds the structure stronger, resulting in a slight decrease of

149 the unit cell. The hybrid functionals HSE06 and PBE0 output similar values, which are again extremely
150 close to experiments, whereas B3LYP predicts a slightly larger unit cell.

151 Again, the bulk modulus was calculated. The discrepancies between the calculated and experimental
152 values were somewhat larger than for rutile. While the experimental value is known to be
153 179 GPa [49], the best theoretical result of 205.7 GPa was found by PBE. All other approaches
154 produced even larger discrepancies, where similar trends to the rutile case are observed. When larger
155 Hubbard parameters are used, the bulk modulus increased and the addition of the Grimme D3
156 correction increases the bulk modulus even further. Hybrid functionals PBE0 and HSE06 output similar
157 results, which significantly overestimate the bulk modulus (~32 %), whereas B3LYP overshoots for
158 24 %. Other literature reports list the following values for the bulk modulus of anatase: 221 Å (GGA)
159 [53], 199.5 Å (LDA), 179.8 Å (GGA) [54], 201 Å (LDA), 183 Å (GGA) [55] and 193 Å (hybrid B3LYP) [56].

3.2 Electronic properties

We now turn our attention to the electronic properties, which have been a challenge for DFT when describing semiconductors. Since local functionals in LDA and GGA approximations severely underestimate the band gap of semiconductors [23]. Therefore, we use DFT+U and hybrid functionals to study the electronic properties of anatase and rutile.

Rutile TiO_2 exhibits a direct (Γ-Γ) band gap with an experimental value of 3.0 eV [57], whereas anatase is an indirect (M-Γ) semiconductor with an experimental band gap of 3.2 eV [58].

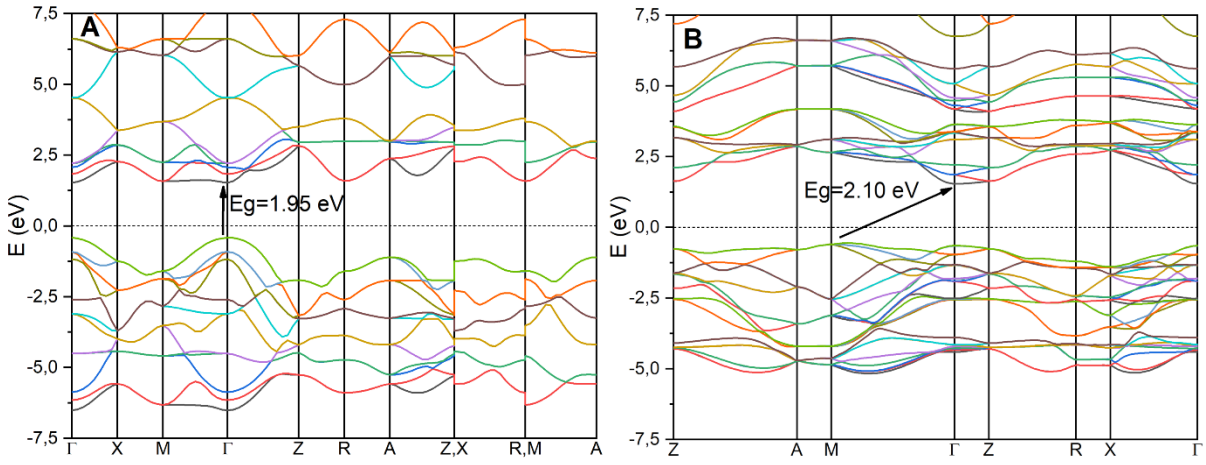

Figure 1: Bandstructure obtained with PBE for A) rutile (direct band gap) and B) anatase (indirect band gap). The dotted line represents the fermi level.

In Figure 1, we display the calculated band structures for rutile and anatase with PBE. While PBE correctly captures the semiconductor character of TiO_2, there is no quantitative agreement as the

band gap is underestimated by more than 1 eV. The use of the Hubbard correction somewhat improves the calculated structure, as shown in Figure 2.

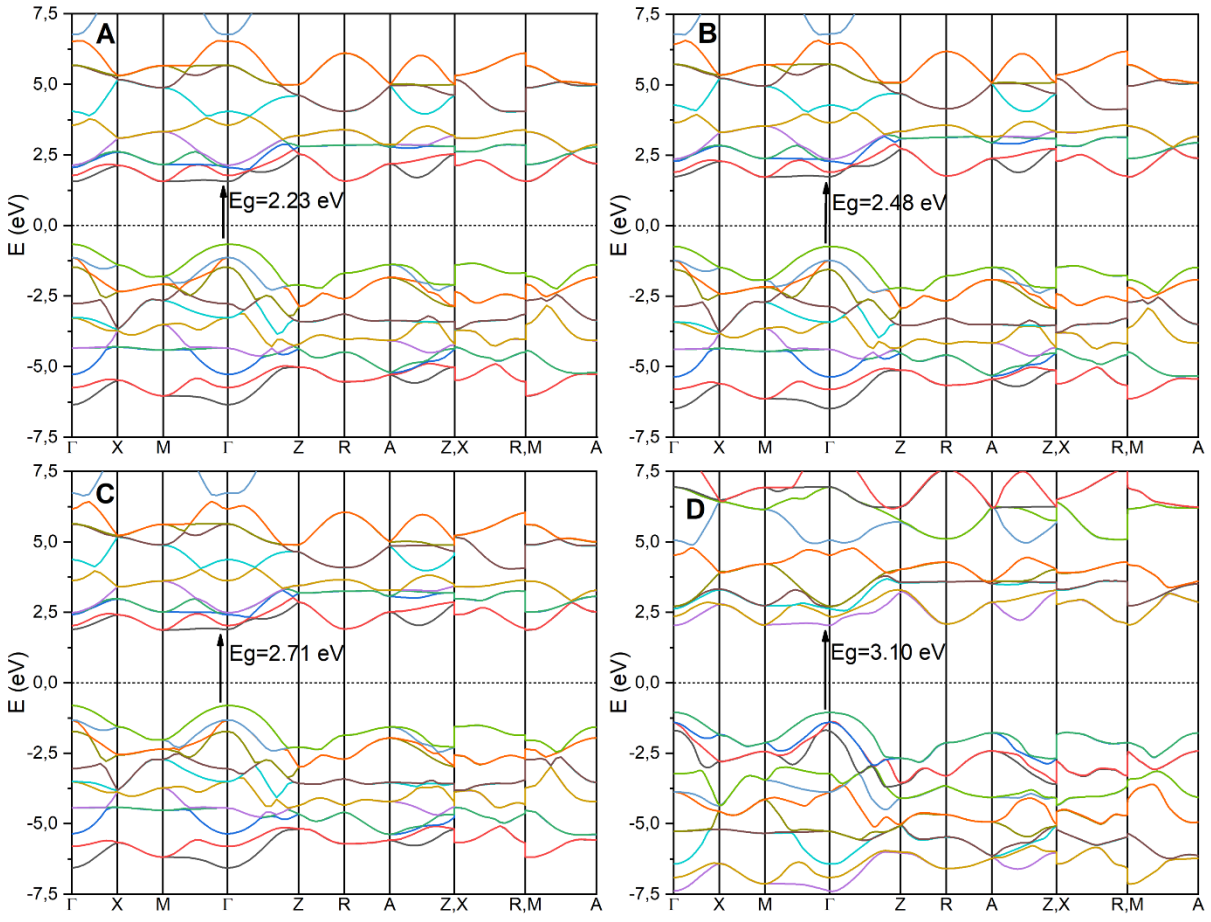

Figure 2: Bandstructure of rutile TiO_2 obtained by A) PBE+4, B) PBE+6, C) PBE+8 and D) HSE06 functionals. The dotted line represents the fermi level.

The *U-J* value of 4 eV increases the band gap from 1.95 eV (PBE) to 2.23 eV, which is further increased to 2.48 eV for *U-J* = 6 eV and finally to 2.71 eV for 8 eV, which is still less than the experimental value. The hybrid functional HSE06 yields a band gap of 3.10 eV, which is consistent with the experimental value of 3.0 eV. For anatase, similar trends were observed (not shown). The calculated (indirect) band gaps are 2.10, 2.55, 2.73, 2.97 and 3.34 eV for PBE, PBE+4, PBE+6, PBE+8 and HSE06, respectively, while the experimental value is 3.20 eV. This is consistent with the literature reports on optimal *U-J* values for band gap calculations ranging between 8-10 eV for both rutile and anatase [57, 58].

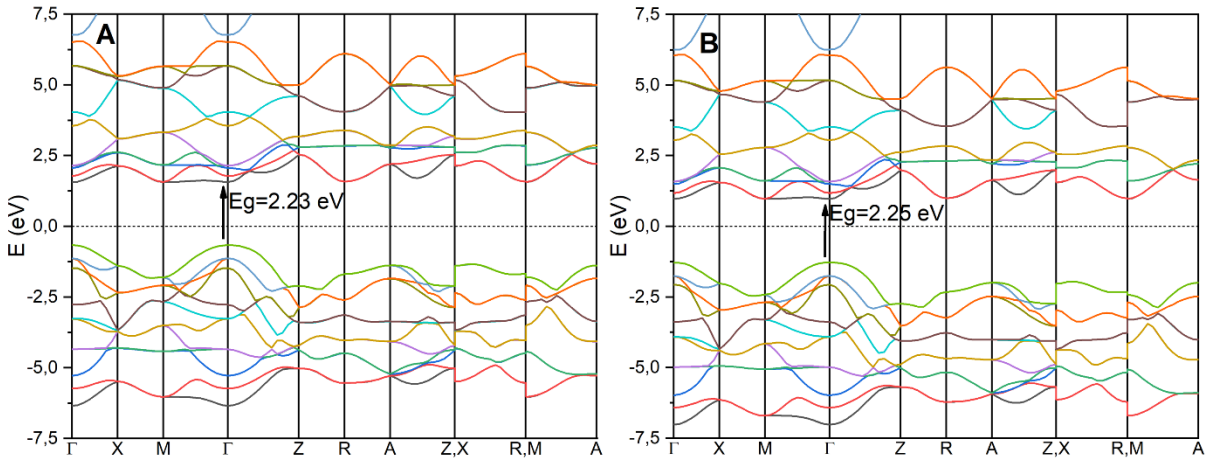

Figure 3: Bandstructure of rutile TiO_2 obtained with A) PBE+4 and B) PBE+4+D3. The dotted line represents the fermi level.

The Grimme D3 correction has little to no effect on the electronic structure (see Figure 3) and thus the band gap.

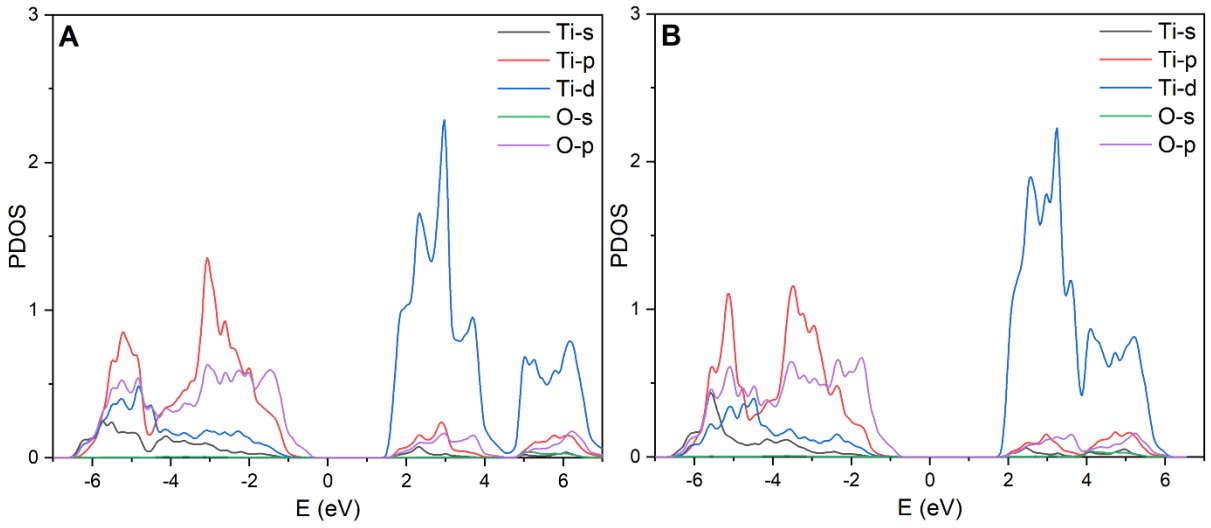

Figure 4: The projected density of states on A) PBE and B) PBE+8 rutile TiO_2. The fermi level is set at 0 eV.

From the band gap structure, the effective mass of photogenerate electrons and holes was estimated. For anatase and rutile, the calculated effective mass of electrons is m_e*(G→Z)=0.15m_0, m_e*(G→M)=0.05m_0 and m_e*(G→Z)=0.14m_0, m_e*(G→M)=0.08m_0, respectively. The calculated effective mass of holes is m_e*(G→Z)=0.20m_0, m_e*(G→M)=0.20m_0 and m_e*(G→Z)=1.10m_0, m_e*(G→M)=0.15m_0, respectively. The values vary negligibly if PBE or HSE06 is used and are consistent with the work of Zhang et al. [36] This explains the better photoactivity of anatase, which has a lighter

and thus more mobile charge carriers, which can more easily diffuse and exhibit a lower recombination rate.

Another important property of a catalyst is the (projected) density of states (PDOS). In Figure 4, we show the PDOS for rutile at the PBE and PBE+8 level. Evidently the valence band is mostly composed of Ti-*p* and O-*p* states, whereas the conduction band is mainly composed of Ti-*d* states. This is consistent with the results from Han et al. [61], where they also identified a near separation between the higher and lower conduction band with the PBE functional, which is in our case visible at about 4.6 eV above the Fermi level. However, this artifact disappears upon the use of the Hubbard correction, evidenced as an overlap between the lower and higher-lying portions of the conduction band, which Han et al. attributed to the better band gap predictions.

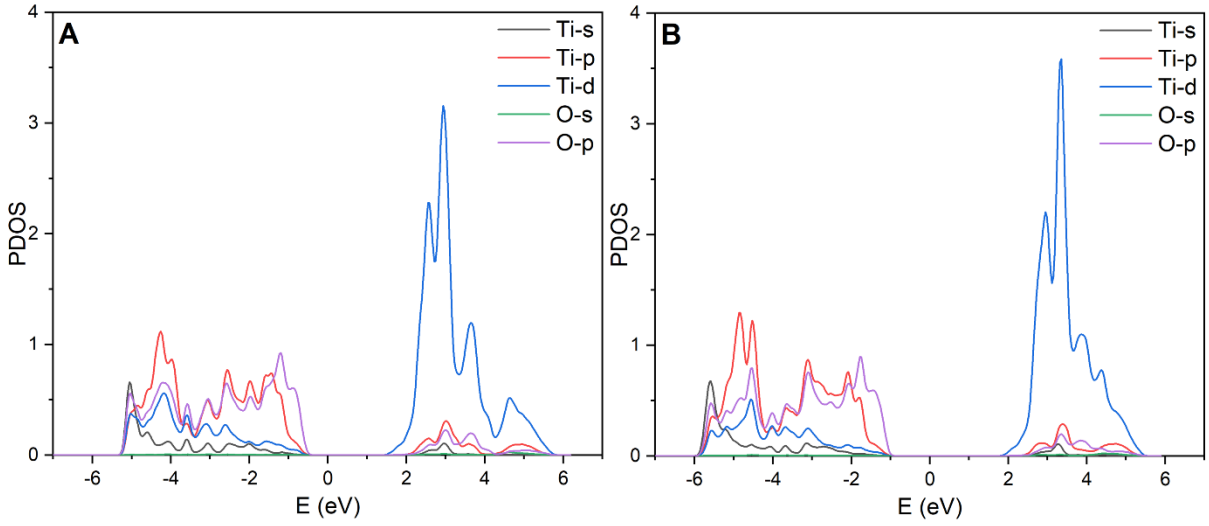

Figure 5: The projected density of states on a) PBE and b) PBE+8 anatase TiO_2. The fermi level is set at 0 eV.

Similar to rutile, the valence band minimum (VBM) of anatase is composed of O-*p* states, whereas the conduction band maximum (CBM) is mostly Ti-*d* states (see Figure 5). The valence band is mainly composed of a mixture of O-*p* and Ti-*p* states, whereas the conduction band is mainly composed of Ti-d states. Compared to rutile, we can observe a softer quasi separation of the conduction band states at about 4.2 eV above the Fermi level for PBE, which the Hubbard correction removes.

Table 3: Calculated band gap in eV and in the brackets the relative deviation versus the experimental value.

	Rutile	Anatase
Exp.	3.0 [57]	3.2 [58]
PBE	1.95 (-35 %)	2.10 (-34 %)
PBE+4	2.23 (-26 %)	2.55 (-20 %)
PBE+6	2.48 (-17 %)	2.73 (-15 %)
PBE+8	2.71 (-9.7 %)	2.97 (-7.2 %)
PBE+4+D3	2.25 (-25 %)	2.50 (-22 %)
PBE+6+D3	2.48 (-17 %)	2.72 (-15 %)
PBE+8+D3	2.73 (-9.0 %)	2.98 (-6.9 %)
PBE0	3.82 (+27 %)	4.05 (+27 %)
HSE06	3.10 (+ 3.3 %)	3.34 (+4.4 %)
B3LYP	3.35 (+ 12 %)	3.59 (+12 %)

The calculated band gaps for all approaches are summarized in Table 3. Increasing the *U-J* value clearly improves the predicted band gap values, which approach the experimental values at the *U-J* parameter of around 8-10 eV [57, 60]. Nonetheless, the band gap is not the sole property one would wish to reproduce, making a unified choice of the *U-J* value problematic. In the literature, different values of U-J ranging from 3 to 5 eV were used for researching defects [61, 62], interactions [65], dopants [64, 65] and structures. The choice of U value is highly sensitive as emphasized by Liu et al. [66]. It should be kept in mind that the *U-J* values above 7 eV might produce physically meaningless results due to breaking of the physical background of DFT+U.

Hybrid functionals *can* offset their huge computational cost by generating accurate results provided they have been properly parametrized for the task at hand. PBE0 produces poor results, overestimating the band gap by roughly 26 % for both rutile and anatase. B3LYP offers a much better

agreement with errors of roughly 12 %, whereas HSE06 performs best, differing from the experimental values for rutile and anatase by 3.3 and 4.4 %, respectively.

3.3 Optical properties

For the photocatalytic performance of TiO_2 polymorphs, optical properties are most important. In this section, we focus on rutile and anatase. Since both are anisotropic materials, their properties differ depending on the direction. For instance, optical properties in the *c* direction (ε∥c) differ from those in the *ab* plane (ε⊥c). The calculated dielectric constants at 0 eV are presented in Table 4, together with the experimental values and previous theoretical results.

Table 4: Calculated dielectric constants of rutile and anatase TiO_2. Scissoring (in our work) is taken into account unless otherwise specified.

	Rutile		Anatase	
	ε⊥c	ε∥c	ε⊥c	ε∥c
Exp.	5.70	7.00	5.80	5.40
PBE	5.55 (-2.6 %)	6.63 (-5.3 %)	4.63 (-20.2 %)	4.38 (-18.9 %)
PBE (no scissoring)	6.64 (+16.5 %)	8.03 (+14.7 %)	5.49 (-5.3 %)	5.10 (-5.6 %)
PBE+4	5.29 (-7.2 %)	6.22 (-11.1 %)	4.31 (-25.7 %)	4.15 (-23.1 %)
PBE+6	5.11 (+10.4 %)	5.96 (-14.9 %)	4.17 (-28.1 %)	4.04 (-25.2 %)
PBE+8	4.98 (+12.6 %)	5.78 (-17.4 %)	4.08 (-29.7 %)	3.97 (-26.5 %)
PBE+4+D3	5.30 (+7.0 %)	6.19 (-11.6 %)	4.25 (-26.7 %)	4.08 (-24.4 %)
PBE+6+D3	5.14 (+9.8 %)	5.97 (-14.7 %)	4.16 (-28.3 %)	4.03 (-25.4 %)
PBE+8+D3	4.99 (+12.5 %)	5.77 (-17.6 %)	4.08 (-29.7 %)	3.94 (-27.0 %)
BSE [3]	5.71 (+0.2 %)	7.33 (+4.7 %)	5.12 (-11.7 %)	4.98 (-7.8 %)
LDA [68]	7.61 (+33.5 %)	9.01 (+28.7 %)	6.99 (+20.5 %)	6.66 (+23.3 %)
GGA [68]	7.34 (+28.8 %)	8.68 (+24.0 %)	6.75 (+16.4 %)	6.44 (+19.3 %)
mBJ [68]	5.75 (+0.9 %)	6.70 (-4.3 %)	5.35 (-7.8 %)	5.21 (-3.5 %)

For rutile, PBE predicts the values of 5.55 and 6.63 for ε⊥c and ε∥c, which is close to the experimental values of 5.70 and 7.00, respectively. In the case of anatase, they are underestimated at 4.63 and 4.38 relative to experimental values of 5.80 and 5.40 for ε⊥c and ε∥c, respectively. The results were obtained with the application of the scissoring operator, which artificially expands the band gap to the experimentally determined values. We observe that the exclusion of scissoring operator results in higher, physically meaningless values. This is explained by the Penn model [69], where the dielectric constant is inversely proportional to the band gap.

Another crucial parameter is the number of bands included in the calculation. In the case of rutile, increasing the number of bands from 33 to 48 results in a significant increase from 5.71 to 6.54 (scissoring operator not applied). Therefore, choosing the correct methodology is of vital importance. For subsequent results, the scissoring operator was applied and the number of bands was four times the number of occupied bands.

The introduction of the Hubbard parameter on top of PBE seems to steadily decrease the dielectric constant. Furthermore, similar trends as for rutile can be observed for anatase, although the results are further away from the experimental value. Comparing PBE+U to PBE+U+D3 results shows that the Grimme D3 correction has no effect on the dielectric constant, as expected. Literature reports on the dielectric constants vary, which might be due to the choice of functionals (LDA, GGA …) or the convergence procedure. Comparing our PBE results with GGA results by Sai et al. [68], we observe a considerable overestimation with 7.34 for ε⊥c (rutile). Comparing our calculated values (RPA) with the standard and more expensive Bethe-Salpeter equation (BSE) by Zhu et al. [3] or mBJ by Gong et al. [68], we observe that in the case of anatase, BSE and mBJ also underestimate the dielectric constant in both planes. We can therefore conclude that RPA results can provide a reasonable agreement with the experimental data at a significantly lower computational cost.

Furthermore, a calculation of the dielectric response function was conducted in an energy range span of 0-12 eV, as shown in Figure 6. Since the dispersion correction has negligible effect on the optical properties, those calculations are not shown.

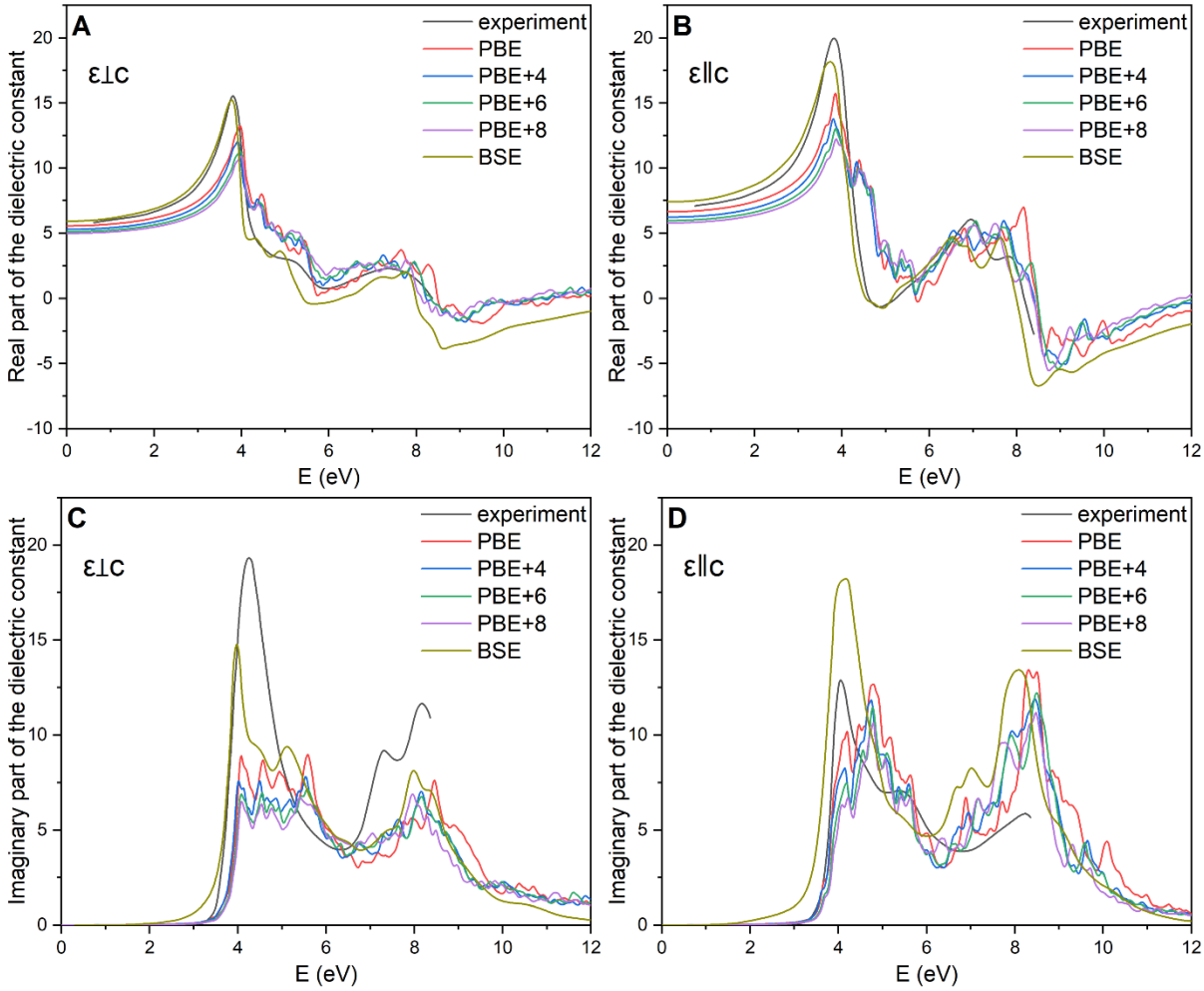

Figure 6: The dielectric response for rutile in the energy span from 0-12 eV for real part of dielectric response for A) ε⊥c and B) ε∥c and imaginary part of dielectric response for C) ε⊥c and D) ε∥c. BSE values obtained from Reference [3].

For rutile, ε⊥c has the first peak at about 3.8 eV, which is well reproduced by BSE but slightly shifted towards higher energies (+0.2 eV) for PBE and PBE+U. Overall, BSE exhibits a slightly better agreement with the experiment but the PBE and PBE+U results are comparable. Similar trends are observed for ε∥c, where BSE outperforms RPA, but RPA still offers reasonable agreement with the experimental data. In the imaginary part of the dielectric response, larger discrepancies can be observed. For ε⊥c, BSE predicts optical absorption at lower energies than experimentally observed, whereas RPA results

offer a better agreement. Nevertheless, the first peaks roughly overlap, but the general shape of the experimental spectrum overall is better reproduced by BSE. The first peak occurring at about 4.3 eV in the experiment is predicted at roughly 3.8 eV with BSE, whereas RPA predicts several alternating peaks in that range. Above 5 eV, BSE and RPA yield similar results. Comparable trends are discovered for the ε‖c case.

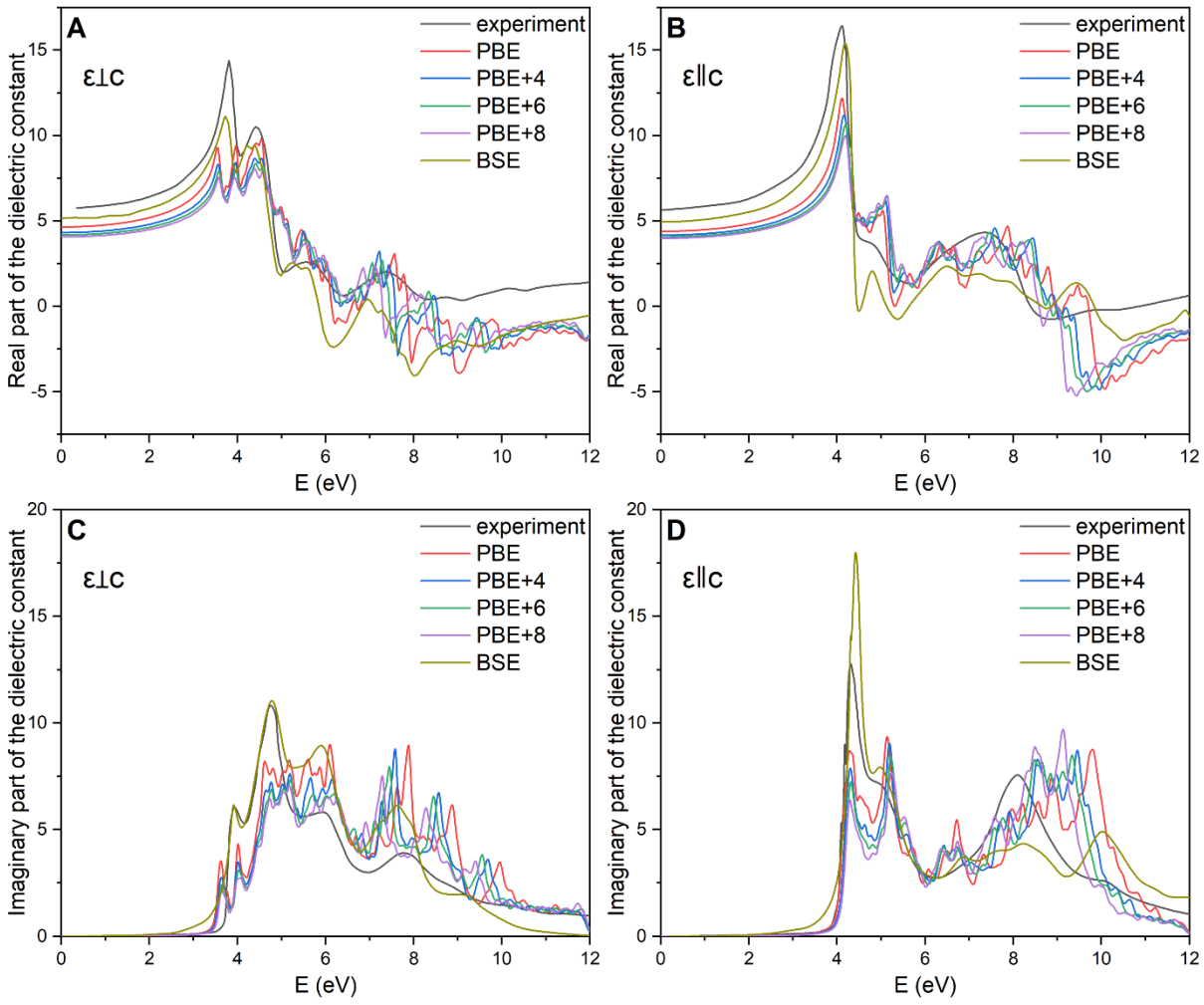

Figure 7: The dielectric response for anatase in the energy span from 0-12 eV for real part of dielectric response for A) ε⊥c and B) ε‖c and imaginary part of dielectric response for C) ε⊥c and D) ε‖c. BSE values obtained from reference [3].

The calculated dielectric constants for anatase are shown in Figure 7. All approaches underestimate the real part of the dielectric constant at E = 0 eV for anatase. Again, we can see that BSE offers superior results in comparison with RPA for both real and imaginary part of the dielectric response.

Again, the imaginary component from BSE of the dielectric response predicts a faster absorption relative to the experiment and RPA. The results agree well with the previous work by Asahi et al. [70]

3.4 CO_2 adsorption on pristine rutile and anatase surfaces

Lastly, we focus on CO_2 adsorption. For TiO_2 to be useful as a photocatalyst for CO_2 reduction, it should sufficiently bind and activate CO_2. Based on literature data [69, 70] on the most frequently exposed surfaces of anatase and rutile TiO_2, we investigated the (001), (101) and (011) surfaces of anatase and the (101), (001) and (110) surfaces of rutile. The adsorption was investigated at the PBE, PBE+4 and PBE+4+D3 levels.

3.4.1 Anatase

We identified four distinct physisorption configurations for CO_2 on all anatase surfaces, shown in Figure 8 as CO_2-0, CO_2-1, CO_2-2 and CO_2-3.

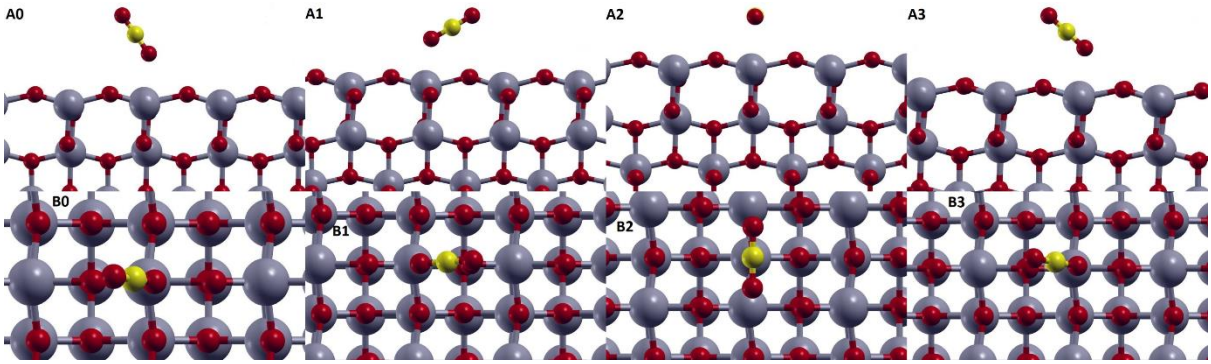

Figure 8: Adsorption of CO_2 on anatase (001), where A represents side view, B is the top view and 1, 2, 3, 4 denote the respective adsorption configuration. Colour code: grey-Ti, red-O and yellow-C.

In all instances, the CO_2 molecule retains its linear shape and adsorbs either at an angle (CO_2-0, CO_2-1, CO_2-3) or lying flat (CO_2-2). The adsorption energies, the titanium-oxygen (from CO_2) distance and the CO_2 angle are summarized in .

.

Table 5: Adsorption energies (in eV), Ti-O bond length (Å) and OCO angle (°) for different CO_2 adsorption modes on the anatase (001) surface.

	PBE			PBE+4			PBE+4+D3		
	E_{ads}	Ti-O	Angle	E_{ads}	Ti-O (Å)	Angle	E_{ads}	Ti-O	Angle
CO_2-0	-0.25	2.421	179.4	-0.27	2.369	179.1	-0.42	2.355	179
CO_2-1	-0.30	2.305	177.7	-0.32	2.287	177.6	-0.49	2.303	177.5
CO_2-2	-0.19	2.663	177.0	-0.19	2.738	177.1	-0.39	2.762	177.5
CO_2-3	-0.25	2.370	179.7	-0.28	2.401	179.4	-0.44	2.335	179.1

PBE and PBE+4 predict a weak interaction of CO_2 with the surface (below 0.32 eV), which implies that physisorption is the main mechanism. If we include the Grimme D3 dispersion correction, the interaction is approximately 0.2 ev stronger, reaching –0.49 eV. In all cases, there is no geometric distortion as the molecule is merely physisorbed and there is negligible charge transfer. Literature data on pristine anatase (001) surfaces is scarce. Using hybrid PBE0, Mino et al. [73] calculated a bent structure with an adsorption energy of -1.31 eV.

For the anatase (101) surface, the adsorption configurations are shown in **Error! Reference source not found.**1. As is the case for anatase (001) the CO_2 molecule retains its linear form and binds in a tilted position. As shown in **Error! Reference source not found.**1, CO_2 binds slightly more strongly to the (101) surface, reaching -0.58 eV (with PBE+4+D3), which is consistent with the work from Sorescu et al. [74] who studied the adsorption of CO_2 on pristine anatase (101) surface using a PBE functional with the Tkatchenko-Scheffler correction for the long range interactions. They calculated the most stable adsorption configurations to be the linear CO_2 with an interaction of -0.48 eV. Mino et al. [73] investigated the adsorption energies of CO_2 using the hybrid functional PBE0. Their value range from -0.25 eV and -0.41 eV. In all cases, this is the case of physisorption.

On the anatase (011) surface, the molecule retains its linear shape and adsorbs at an angle over a Ti atom (see Figure S2). The adsorption energies, titanium-oxygen (from CO_2) distance and the CO_2 angles are summarized in **Error! Reference source not found.**S2. The adsorption interaction is reaches -0.60 eV in the PBE+4+D3 approach.

The inability to identify any activated CO_2 configurations on any anatase surface leads us to conclude that (undoped) anatase would perform poorly as a catalyst for CO_2 photoreduction despite its greater photoactivity.

3.4.2 Rutile

Lastly, we turn our attention to rutile surfaces. Four adsorption configurations for CO_2 were determined on the rutile (110) and rutile (101) surfaces, denoted as CO_2-0, CO_2-1, CO_2-2 and CO_2-3. In all instances the CO_2 molecule retains its linearity (see Figure S3) and is adsorbed on the titanium atom at different angles. The adsorption energies, the Ti-O distances and the CO_2 angle are summarized in **Error! Reference source not found.**3. All sites on rutle (110) exhibit similar interaction strengths, which were calculated around -0.3 eV at the PBE level, -0.4 eV at the PBE+4 level and -0.65 eV with the Grimme D3 correction. Our results are in good agreement with Sorescu et al.,[63] who obtained -0.38 eV using the Grimme correction and --0.43 eV using the Tkatchenko Scheffler correction.

The adsorption structures on rutile (101) are shown in Figure S4. Again, the interaction is typical of physisorption with energies around 0.3 eV at the PBE level and 0.56 eV at the PBE+U+D3 level (see Table S4). To the best of our knowledge, no literature reports yet exist of CO_2 adsorption on the pristine rutile (101) surface.

These interactions are physisorptions of CO_2 in the linear configuration with no activation, which is illustrated by low adsorption energies and is confirmed by the Bader charge analysis, showing no charge transfer, and PDOS, showing little orbital overlap.

3.1.1 Chemisorption on rutile(001)

On the rutile(001) surface, three distinct adsorption configurations were identified, marked as CO_2-0, CO_2-1 and CO_2-2. Among those, CO_2 is activated in the CO_2-0. The molecule is adsorbed in a bent configuration, where the carbon atom binds to the surface oxygen and the oxygen atom from CO_2 binds to surface Ti. The results are congruent with a report by Jiang et al. [75], where the (001) surface exhibited higher energy, relative to (111) and (110), hinting that it could be more active. The adsorption configurations are presented in Figure 9, while the adsorption energies, CO_2 angles and distances are summarized in Table 6.

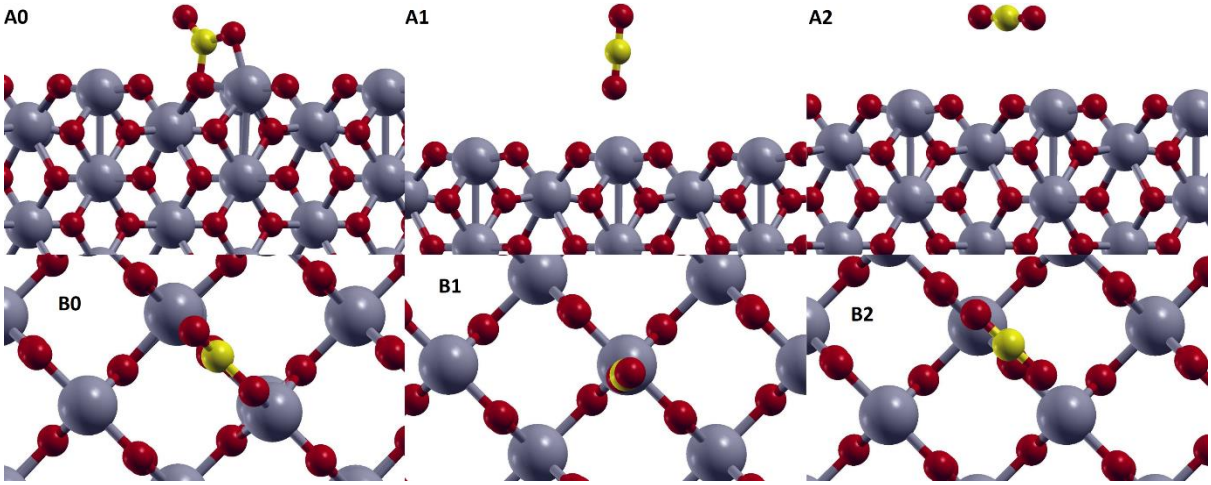

Figure 9: Adsorption of CO_2 on rutile (001), where A represents side view, B is the top view and 1, 2, 3 denote the respective adsorption configuration. Colour code: grey-Ti, red-O and yellow-C.

Table 6: Adsorption energies (eV), Ti-O bond length (Å) and angle (°) for different CO_2 adsorptions for PBE, PBE+4 and PBE+4+D3 on rutile (001) surface.

	PBE			PBE+4			PBE+4+D3		
	E_{ads}	Ti-O	Angle	E_{ads}	Ti-O	Angle	E_{ads}	Ti-O	Angle
CO_2-0	-1.17	1.924	125.9	-1.21	1.945	126.4	-1.45	1.943	126.8
CO_2-1	-0.21	2.392	179.3	-0.23	2.389	179.3	-0.35	2.354	179.3
CO_2-2	-0.08	3.350	177.9	-0.09	3.330	177.9	-0.26	3.326	177.6

In the CO_2-0 configuration, CO_2 is strongly adsorbed to the surface (-1.2 eV at the PBE level, -1.45 eV at the PBE+U). The bond between the surface Ti and O (from CO_2) is shortened by roughly 0.4 Å compared to physisorbed CO_2, proving stronger interaction. We see that CO_2 is strongly deformed with the C-O-C angle of 126°. Bader charge analysis showed that there is non-negligible electron transfer (Table 7). While the charge transfer is negligible in the case of physisorbed CO_2, the chemisorbed CO_2 is activated as $0.2e_0^-$ flows from the catalyst to the molecule. The effects of this activation were further probed by calculating the PDOS for the activated CO_2-0 and un-activated CO_2-1 configuration.

Table 7: Bader charge analysis of CO_2 adsorption on rutile 001 surface in |e| relative to unadsorbed CO_2.

	PBE	PBE+4	PBE+4+D3
CO_2-0	-0.166	-0.213	-0.203
CO_2-1	0.005	0.003	0.005
CO_2-2	-0.023	-0.026	-0.026

We observe a significantly higher overlap in the valence band between the surface and adsorbed CO_2 in the activated configuration in comparison to the un-activated (Figure 10). This indicates substantial hybridization, resulting in stronger bonding and greater reactivity.

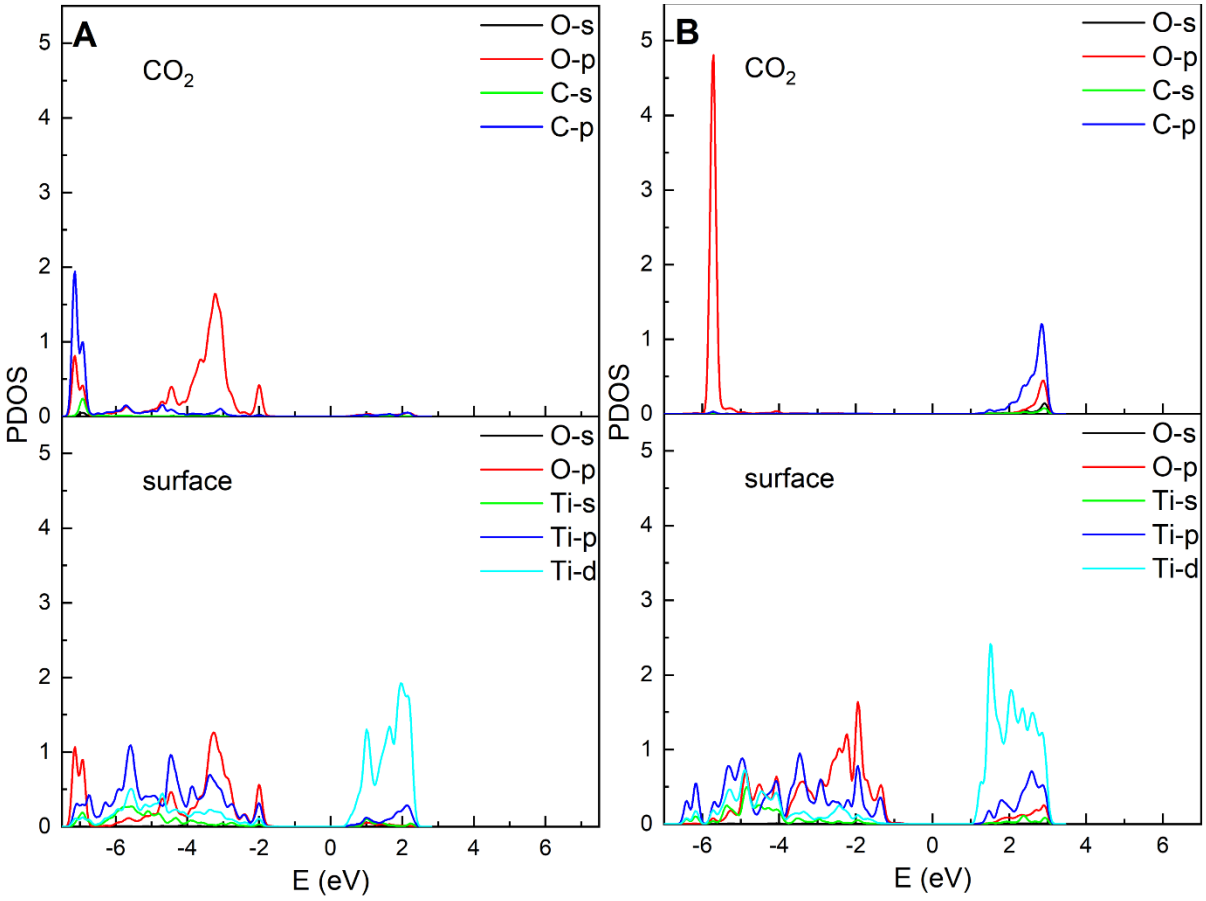

Figure 10: Projected density of states of the adsorbed CO_2 (top) and surface (bottom) of A) CO_2-0 and B) CO_2-1 configuration with the PBE+4 functional. The Fermi level is set at 0 eV.

As expected, PBE predicts the lowest adsorption energies irrespective of the Hubbard correction used. To obtain results comparable to higher methods (hybrids), dispersion correction (D3) was found to be adequate. The effect on the geometry is weak and usually reduces the distance between the adsorbed molecule and the corresponding surface site. On the other hand, when the molecule adsorbs in a bent shape, as was the case for the rutile (001) surface, it gets activated.

4. Conclusions

Properties of rutile and anatase TiO_2 were studied due to their potential photocatalytic activity in CO_2 reduction. Their unit cell was optimized using GGA (PBE, PBE+U (*U-J* = 4, 6, 8 eV), PBE+U+D3)

functionals as well as hybrids (PBE0, HSE06, B3LYP). The results are consistent with the experimental data. The Hubbard correction slightly elongates the lattice proportionately to the U value. The Grimme D3 correction slightly compresses the lattice due to inclusion of long range attractive forces (dispersion). B3LYP in general predicted slightly bigger bulk structures relative to PBE0 and HSE06. The results show that inexpensive GGA functionals suffice for geometric optimizations. Moreover, bulk moduli were calculated. We showed that while the PBE, PBE+U and PBE+U+D3 results are comparable, hybrid functionals generally considerably overestimate the bulk modulus. Vanilla PBE actually produced results closest to the experimental value.

Subsequently, electronic properties (band gap, band structure and effective mass of charge carriers) were calculated for rutile and anatase. It is well known that the standard GGA functionals severely underestimate the band gap for semiconductors, which is also the case for TiO_2. The use of Hubbard approach improved the results proportionately to the *U-J* value. Higher values better reproduced larger band gaps but for best agreement dangerously high *U-J* values were required. It should be noted that the choice of the *U-J* value is not trivial because different properties are best reproduced with *different U-J* values. The Grimme D3 correction has almost no effect on the electronic properties. We benchmarked the inexepensive GGA functionals and the hybrids PBE0, B3LYP and HSE06, where HSE06 demonstrated the best results and very well justifies the accuracy/computational cost trade-off, whereas PBE0 and B3LYP do not.

Optical properties were also investigated and it was found that the correct methodology and convergence tests are crucial for viable results. RPA results, which do not include electron hole interaction, were benchmarked against BSE (electron-hole screening included). It was found that BSE slightly outperforms RPA, however at a much higher computational cost. The dielectric constant calculations revealed that RPA is not far off and even predicts the optical absorption onset better than BSE.

Finally, we investigated the adsorption of CO_2 on different surfaces planes for rutile and anatase since the photocatalytic activity is dependent not only on the catalyst type but also on the exposed surface. We therefore identified the three most commonly expressed surfaces for both rutile and anatase. Different CO_2 configurations were relaxed and compared on all surfaces with the PBE, PBE+U and PBE+U+D3 (*U-J* = 4 eV) methodologies. CO_2 mostly physisorbs with the interaction strength of 0.5 eV, where the molecule is not activated as evidenced by no charge transfer, PDOS analysis and the molecule linear shape. The results are in line with previous literature, where the pristine TiO_2 surfaces exhibit weak interaction with CO_2, manifesting as low adsorption energies.

The only surface that activated the CO_2 molecule (strong adsorption, charge transfer and bending of CO_2) was the rutile (001) surface. The results revealed that PBE predicts the weakest adsorption energies, which slightly increase with the Hubbard correction (U), whereas the inclusion of Grimme D3 correction exhibits higher adsorption energies. As these corrected values more closely correspond to (literature) data from the hybrid calculation, dispersion forces must play a significant role in the process.

Overall, we show that for the description of TiO_2 properties and the interaction with CO_2, the choice of the functional is paramount. More expensive hybrid functionals do not necessarily outperform cheaper GGA functionals. HSE06 performs rather well, while PBE0 and B3LYP are less suitable for describing periodic semiconducting systems. In many cases, however, cheaper GGA+U methods serve as a capable surrogate.

Acknowledgements

The authors thank the European Union for financial support through Grant agreement No. 814416 (ReaxPro) under the auspices of the Framework Program for Research and Innovation Horizon 2020.

The Slovenian Research Agency (ARRS) supported parts of this work through Core Funding P2-0152 and Grant J2-1724. M.H. also acknowledges the Infrastructure Grant I0-0039 (IP GZM) by ARRS.

References

[1] A.J. Haider, Z.N. Jameel, I.H.M. Al-Hussaini, Review on: Titanium dioxide applications, Energy Procedia. 157 (2019) 17–29. https://doi.org/10.1016/j.egypro.2018.11.159.

[2] S. Mo, W.Y. Ching, Electronic and optical properties of three phases of titanium dioxide: Rutile, anatase, and brookite, Phys. Rev. B. 51 (1995) 13023–13032.

[3] T. Zhu, S.P. Gao, The stability, electronic structure, and optical property of tio2 polymorphs, J. Phys. Chem. C. 118 (2014) 11385–11396. https://doi.org/10.1021/jp412462m.

[4] X. Wang, F. Wang, Y. Sang, H. Liu, Full-Spectrum Solar-Light-Activated Photocatalysts for Light – Chemical Energy Conversion, Adv. Energy Mater. 7 (2017) 1700473. https://doi.org/10.1002/aenm.201700473.

[5] X. Li, Z. Zhuang, W. Li, H. Pan, Photocatalytic reduction of CO2over noble metal-loaded and nitrogen-doped mesoporous TiO2, Appl. Catal. A Gen. 429–430 (2012) 31–38. https://doi.org/10.1016/j.apcata.2012.04.001.

[6] C. Yi, Q. Liao, W. Deng, Y. Huang, J. Mao, B. Zhang, G. Wu, The preparation of amorphous TiO2 doped with cationic S and its application to the degradation of DCFs under visible light irradiation, Sci. Total Environ. 684 (2019) 527–536. https://doi.org/10.1016/j.scitotenv.2019.05.338.

[7] J. Shao, W. Sheng, M. Wang, S. Li, J. Chen, Y. Zhang, S. Cao, In situ synthesis of carbon-doped TiO2 single-crystal nanorods with a remarkably photocatalytic efficiency, Appl. Catal. B Environ. 209 (2017) 311–319. https://doi.org/10.1016/j.apcatb.2017.03.008.

[8] K.K. Ghuman, C.V. Singh, Effect of doping on electronic structure and photocatalytic behavior

of amorphous TiO2, J. Phys. Condens. Matter. 25 (2013) 475501. https://doi.org/10.1088/0953-8984/25/47/475501.

[9] X. Ma, Y. Wu, Y. Lu, J. Xu, Y. Wang, Y. Zhu, Effect of compensated codoping on the photoelectrochemical properties of anatase TiO2 photocatalyst, J. Phys. Chem. C. 115 (2011) 16963–16969. https://doi.org/10.1021/jp202750w.

[10] F. Wang, Z. Ma, P. Ban, X. Xu, C, N and S codoped rutile TiO2 nanorods for enhanced visible-light photocatalytic activity, Mater. Lett. 195 (2017) 143–146. https://doi.org/10.1016/j.matlet.2017.02.113.

[11] V. Subramanian, E.E. Wolf, P. V. Kamat, Catalysis with TiO2/Gold Nanocomposites. Effect of Metal Particle Size on the Fermi Level Equilibration, J. Am. Chem. Soc. 126 (2004) 4943–4950. https://doi.org/10.1021/ja0315199.

[12] T.T.Y. Tan, C.K. Yip, D. Beydoun, R. Amal, Effects of nano-Ag particles loading on TiO 2 photocatalytic reduction of selenate ions, Chem. Eng. J. 95 (2003) 179–186. https://doi.org/10.1016/S1385-8947(03)00103-7.

[13] A.T. Montoya, E.G. Gillan, Enhanced Photocatalytic Hydrogen Evolution from Transition-Metal Surface-Modified TiO2, ACS Omega. 3 (2018) 2947–2955. https://doi.org/10.1021/acsomega.7b02021.

[14] R. Dholam, N. Patel, M. Adami, A. Miotello, Hydrogen production by photocatalytic water-splitting using Cr- or Fe-doped TiO2 composite thin films photocatalyst, Int. J. Hydrogen Energy. 34 (2009) 5337–5346. https://doi.org/10.1016/j.ijhydene.2009.05.011.

[15] B. Banerjee, V. Amoli, A. Maurya, A.K. Sinha, A. Bhaumik, Green synthesis of Pt-doped TiO2 nanocrystals with exposed (001) facets and mesoscopic void space for photo-splitting of water under solar irradiation, Nanoscale. 7 (2015) 10504–10512. https://doi.org/10.1039/c5nr02097b.

[16] J. Jia, H. Wang, Z. Lu, P.G. O'Brien, M. Ghoussoub, P. Duchesne, Z. Zheng, P. Li, Q. Qiao, L. Wang, A. Gu, A.A. Jelle, Y. Dong, Q. Wang, K.K. Ghuman, T. Wood, C. Qian, Y. Shao, C. Qiu, M. Ye, Y. Zhu, Z.H. Lu, P. Zhang, A.S. Helmy, C.V. Singh, N.P. Kherani, D.D. Perovic, G.A. Ozin, Photothermal Catalyst Engineering: Hydrogenation of Gaseous CO 2 with High Activity and Tailored Selectivity, Adv. Sci. 4 (2017) 1700252. https://doi.org/10.1002/advs.201700252.

[17] B. Yu, Y. Zhou, P. Li, W. Tu, P. Li, L. Tang, J. Ye, Z. Zou, Photocatalytic reduction of CO2 over Ag/TiO2 nanocomposites prepared with a simple and rapid silver mirror method, Nanoscale. 8 (2016) 11870–11874. https://doi.org/10.1039/c6nr02547a.

[18] J. Li, M. Zhang, Z. Guan, Q. Li, C. He, J. Yang, Synergistic effect of surface and bulk single-electron-trapped oxygen vacancy of TiO2 in the photocatalytic reduction of CO2, Appl. Catal. B Environ. 206 (2017) 300–307. https://doi.org/10.1016/j.apcatb.2017.01.025.

[19] J. Zhuang, W. Dai, Q. Tian, Z. Li, L. Xie, J. Wang, P. Liu, X. Shi, D. Wang, Photocatalytic degradation of RhB over TiO2 bilayer films: Effect of defects and their location, Langmuir. 26 (2010) 9686–9694. https://doi.org/10.1021/la100302m.

[20] W. Yao, B. Zhang, C. Huang, C. Ma, X. Song, Q. Xu, Synthesis and characterization of high efficiency and stable Ag 3PO 4/TiO 2 visible light photocatalyst for the degradation of methylene blue and rhodamine B solutions, J. Mater. Chem. 22 (2012) 4050–4055. https://doi.org/10.1039/c2jm14410g.

[21] J. Liu, B. Cheng, J. Yu, A new understanding of the photocatalytic mechanism of the direct Z-scheme g-C3N4/TiO2 heterostructure, Phys. Chem. Chem. Phys. 18 (2016) 31175–31183. https://doi.org/10.1039/c6cp06147h.

[22] F. Xu, L. Zhang, B. Cheng, J. Yu, Direct Z-Scheme TiO2/NiS Core-Shell Hybrid Nanofibers with Enhanced Photocatalytic H2-Production Activity, ACS Sustain. Chem. Eng. 6 (2018) 12291–12298. https://doi.org/10.1021/acssuschemeng.8b02710.

[23] Á. Morales-García, R. Valero, F. Illas, An Empirical, yet Practical Way to Predict the Band Gap in Solids by Using Density Functional Band Structure Calculations, J. Phys. Chem. C. 121 (2017) 18862–18866. https://doi.org/10.1021/acs.jpcc.7b07421.

[24] J. Hubbard, P.R.S.L. A, Electron correlations in narrow energy bands, Proc. R. Soc. London. Ser. A. Math. Phys. Sci. 276 (1963) 238–257. https://doi.org/10.1098/rspa.1963.0204.

[25] P. Verma, D.G. Truhlar, Does DFT+U mimic hybrid density functionals?, Theor. Chem. Acc. 135 (2016) 1–15. https://doi.org/10.1007/s00214-016-1927-4.

[26] C. Loschen, J. Carrasco, K.M. Neyman, F. Illas, First-principles LDA+U and GGA+U study of cerium oxides: Dependence on the effective U parameter, Phys. Rev. B - Condens. Matter Mater. Phys. 75 (2007) 1–8. https://doi.org/10.1103/PhysRevB.75.035115.

[27] S. Huygh, A. Bogaerts, E.C. Neyts, How Oxygen Vacancies Activate CO2 Dissociation on TiO2 Anatase (001), J. Phys. Chem. C. 120 (2016) 21659–21669. https://doi.org/10.1021/acs.jpcc.6b07459.

[28] M.S. Akple, J. Low, Z. Qin, S. Wageh, A.A. Al-Ghamdi, J. Yu, S. Liu, Nitrogen-doped TiO2 microsheets with enhanced visible light photocatalytic activity for CO2 reduction, Chinese J. Catal. 36 (2015) 2127–2134. https://doi.org/10.1016/S1872-2067(15)60989-5.

[29] O. Rosseler, M. V. Shankar, M.K. Le Du, L. Schmidlin, N. Keller, V. Keller, Solar light photocatalytic hydrogen production from water over Pt and Au/TiO2(anatase/rutile) photocatalysts: Influence of noble metal and porogen promotion, J. Catal. 269 (2010) 179–190. https://doi.org/10.1016/j.jcat.2009.11.006.

[30] C. Wang, Y. Zhao, H. Xu, Y. Li, Y. Wei, J. Liu, Z. Zhao, Efficient Z-scheme photocatalysts of ultrathin g-C3N4-wrapped Au/TiO2-nanocrystals for enhanced visible-light-driven conversion of CO2 with H2O, Appl. Catal. B Environ. 263 (2020) 118314. https://doi.org/10.1016/j.apcatb.2019.118314.

528 [31] Ş. Neaţu, J.A. Maciá-Agulló, H. Garcia, Solar light photocatalytic CO2 reduction: General
529 considerations and selected bench-mark photocatalysts, Int. J. Mol. Sci. 15 (2014) 5246–5262.
530 https://doi.org/10.3390/ijms15045246.

531 [32] A.K. Singh, K. Mathew, H.L. Zhuang, R.G. Hennig, Computational screening of 2D materials for
532 photocatalysis, J. Phys. Chem. Lett. 6 (2015) 1087–1098. https://doi.org/10.1021/jz502646d.

533 [33] M. Batzill, Fundamental aspects of surface engineering of transition metal oxide
534 photocatalysts, Energy Environ. Sci. 4 (2011) 3275–3286.
535 https://doi.org/10.1039/c1ee01577j.

536 [34] M. Xu, Y. Gao, E.M. Moreno, M. Kunst, M. Muhler, Y. Wang, H. Idriss, C. Wöll, Photocatalytic
537 activity of bulk TiO2 anatase and rutile single crystals using infrared absorption spectroscopy,
538 Phys. Rev. Lett. 106 (2011) 138302. https://doi.org/10.1103/PhysRevLett.106.138302.

539 [35] T. Luttrell, S. Halpegamage, J. Tao, A. Kramer, E. Sutter, M. Batzill, Why is anatase a better
540 photocatalyst than rutile? - Model studies on epitaxial TiO2 films, Sci. Rep. 4 (2015) 4043.
541 https://doi.org/10.1038/srep04043.

542 [36] J. Zhang, P. Zhou, J. Liu, J. Yu, New understanding of the difference of photocatalytic activity
543 among anatase, rutile and brookite TiO2, Phys. Chem. Chem. Phys. 16 (2014) 20382–20386.
544 https://doi.org/10.1039/c4cp02201g.

545 [37] W. Yu, J. Zhang, T. Peng, New insight into the enhanced photocatalytic activity of N-, C- and S-
546 doped ZnO photocatalysts, Appl. Catal. B Environ. 181 (2016) 220–227.
547 https://doi.org/10.1016/j.apcatb.2015.07.031.

548 [38] J. Pan, G. Liu, G.Q. Lu, H.M. Cheng, On the true photoreactivity order of {001}, {010}, and
549 {101} facets of anatase TiO2 crystals, Angew. Chemie - Int. Ed. 50 (2011) 2133–2137.
550 https://doi.org/10.1002/anie.201006057.

551 [39] J.J. Mortensen, L.B. Hansen, K.W. Jacobsen, Real-space grid implementation of the projector

552 augmented wave method, Phys. Rev. B - Condens. Matter Mater. Phys. 71 (2005) 1–11.
553 https://doi.org/10.1103/PhysRevB.71.035109.

554 [40] S.L. Dudarev, G.A. Botton, S.Y. Savrasov, C.J. Humphreys, A.P. Sutton, Electron-energy-loss
555 spectra and the structural stability of nickel oxide: An LSDA+U study, Phys. Rev. B. 57 (1998)
556 1505–1509.

557 [41] S. Grimme, J. Antony, S. Ehrlich, H. Krieg, parametrization of density functional dispersion
558 correction (DFT-D) for the 94 elements H-Pu dispersion correction „ DFT-D … for the 94
559 elements H-Pu, J. Chem. Phys. 132 (2010) 154104. https://doi.org/10.1063/1.3382344.

560 [42] H.J. Monkhorst, J.D. Pack, Special points for Brillouin-zone integrations, Phys. Rev. B. 13
561 (1976) 5188–5192. https://doi.org/10.1103/PhysRevB.16.1748.

562 [43] L. Bengtsson, Dipole correction for surface supercell calculations, Phys. Rev. B - Condens.
563 Matter Mater. Phys. 59 (1999) 12301–12304. https://doi.org/10.1103/physrevb.61.16921.

564 [44] A.B. Alchagirov, J.P. Perdew, J.C. Boettger, R.C. Albers, C. Fiolhais, Reply to '"Comment on
565 'Energy and pressure versus volume: Equations of state motivated by the stabilized jellium
566 model' ,"' Phys. Rev. B. 67 (2003) 026103. https://doi.org/10.1103/PhysRevB.67.026103.

567 [45] S.L. Adler, Quantum theory of the dielectric constant in real solids, Phys. Rev. 126 (1962)
568 413–420. https://doi.org/10.1103/PhysRev.126.413.

569 [46] N. Wiser, Dielectric constant with local field effects included, Phys. Rev. 129 (1963) 62–69.
570 https://doi.org/10.1103/PhysRev.129.62.

571 [47] Z.H. Levine, D.C. Allan, Linear optical response in silicon and germanium including self-energy
572 effects, Phys. Rev. Lett. 63 (1989) 1719–1722. https://doi.org/10.1103/PhysRevLett.63.1719.

573 [48] J.K. Burdett, T. Hughbanks, G.J. Miller, J. V. Smith, J.W. Richardson, Structural-Electronic
574 Relationships in Inorganic Solids: Powder Neutron Diffraction Studies of the Rutile and

575 Anatase Polymorphs of Titanium Dioxide at 15 and 295 K, J. Am. Chem. Soc. 109 (1987) 3639–
576 3646. https://doi.org/10.1021/ja00246a021.

577 [49] T. Arlt, High-pressure polymorphs of anatase TiO 2, Phys. Rev. B. 61 (2000) 414–419.

578 [50] K.M. Glassford, J.R. Chelikowsky, Structural and electronic properties of titanium dioxide,
579 Phys. Rev. B. 46 (1992) 1284.

580 [51] T. Mahmood, C. Cao, W.S. Khan, Z. Usman, F.K. Butt, S. Hussain, Electronic , elastic , optical
581 properties of rutile TiO 2 under pressure : A DFT study, Phys. B Phys. Condens. Matter. 407
582 (2012) 958–965. https://doi.org/10.1016/j.physb.2011.12.114.

583 [52] M. Mikami, S. Nakamura, O. Kitao, H. Arakawa, X. Gonze, First-Principles Study of Titanium
584 Dioxide : Rutile and Anatase, J. Appl. Phys. 39 (2000) 847–850.

585 [53] M. Iuga, G. Steinle-Neumann, J. Meinhardt, Ab-initio simulation of elastic constants for some
586 ceramic materials, Eur. Phys. J. B. 58 (2007) 127–133. https://doi.org/10.1140/epjb/e2007-
587 00209-1.

588 [54] H. Yao, L. Ouyang, W. Ching, Ab Initio Calculation of Elastic Constants of Ceramic Crystals, J.
589 Am. Ceram. Soc. 90 (2007) 3194–3204. https://doi.org/10.1111/j.1551-2916.2007.01931.x.

590 [55] E. Shojaee, M.R. Mohammadizadeh, First-principles elastic and thermal properties of TiO2: a
591 phonon approach, J. Phys. Condens. Matter. 22 (2009) 015401.
592 https://doi.org/10.1088/0953-8984/22/1/015401.

593 [56] A.R. Albuquerque, M.L. Garzim, M.G. Santos, V. Longo, E. Longo, J.R. Sambrano, DFT Study
594 with Inclusion of the Grimme Potential on Anatase TiO2: Structure , Electronic , and
595 Vibrational Analyses, J. Phys. Chem. A. 116 (2012) 11731–11735.
596 https://doi.org/10.1021/jp308318j.

597 [57] J. Pascual, J. Camassel, H. Mathieu, Fine structure in the intrinsic absorption edge of TiO2,

598 Phys. Rev. B. 18 (1978) 5606–5614. https://doi.org/10.1103/PhysRevB.18.5606.

599 [58] H. Tang, H. Berger, P.E. Schmid, F. Levy, Photoluminescence in TiO2 anatase single crystals,
600 Solid State Commun. 87 (1993) 647–850. https://doi.org/https://doi.org/10.1016/0038-
601 1098(93)90427-O.

602 [59] C.I.N. Morgade, G.F. Cabeza, Synergetic interplay between metal (Pt) and nonmetal (C)
603 species in codoped TiO2 : A DFT + U study, Comput. Mater. Sci. 111 (2016) 513–524.
604 https://doi.org/10.1016/j.commatsci.2015.09.065.

605 [60] M.H. Samat, A.M.M. Ali, M.F.M. Taib, O.H. Hassan, M.Z.A. Yahya, Structural and electronic
606 properties of TiO2 polymorphs with effective on-site coulomb repulsion term: DFT+U
607 approaches, Mater. Today Proc. 17 (2019) 472–483.
608 https://doi.org/10.1016/j.matpr.2019.06.482.

609 [61] X. Han, G. Shao, Electronic properties of rutile TiO2 with nonmetal dopants from first
610 principles, J. Phys. Chem. C. 115 (2011) 8274–8282. https://doi.org/10.1021/jp1106586.

611 [62] H. Wu, S. Lin, J. Wu, Effects of nitrogen concentration on N-doped anatase TiO2 : Density
612 functional theory and Hubbard U analysis, J. Alloys Compd. 522 (2012) 46–50.
613 https://doi.org/10.1016/j.jallcom.2012.01.071.

614 [63] D.C. Sorescu, J. Lee, W.A. Al-saidi, K.D. Jordan, CO2 adsorption on TiO2 (110) rutile : Insight
615 from dispersion-corrected density functional theory calculations and scanning tunneling, J.
616 Chem. Phys. 134 (2011) 104707. https://doi.org/10.1063/1.3561300.

617 [64] X. Lin, Y. Yoon, N.G. Petrik, Z. Li, Z. Wang, V. Glezakou, B.D. Kay, I. Lyubinetsky, G.A. Kimmel,
618 R. Rousseau, Z. Dohna, Structure and Dynamics of CO2 on Rutile TiO2 (110) -1 × 1, J. Phys.
619 Chem. C. 116 (2012) 26322–26334. https://doi.org/10.1021/jp308061j.

620 [65] K. Chen, C. Chen, X. Ren, A. Alsaedi, T. Hayat, Interaction mechanism between different facet
621 TiO 2 and U (VI): Experimental and density-functional theory investigation, Chem. Eng. J. 359

(2019) 944–954. https://doi.org/10.1016/j.cej.2018.11.092.

[66] B. Liu, X. Zhao, The synergetic effect of V and Fe-co-doping in TiO 2 studied from the DFT + U first-principle calculation, Appl. Surf. Sci. 399 (2017) 654–662. https://doi.org/10.1016/j.apsusc.2016.12.075.

[67] K.K. Ghuman, C.V. Singh, A DFT + U study of (Rh , Nb) -codoped rutile TiO2, J. Phys. Condens. Matter. 25 (2013) 085501. https://doi.org/10.1088/0953-8984/25/8/085501.

[68] S. Gong, B.G. Liu, Electronic structures and optical properties of TiO 2: Improved density-functional-theory investigation, Chinese Phys. B. 21 (2012) 057104. https://doi.org/10.1088/1674-1056/21/5/057104.

[69] D.R. Penn, Wave-Number-Dependent Dielectric Function of Semiconductors, Phys. Rev. B. 128 (1962) 2093–2097. https://doi.org/10.1103/PhysRev.128.2093.

[70] R. Asahi, Y. Taga, W. Mannstadt, Electronic and optical properties of anatase, Phys. Rev. B - Condens. Matter Mater. Phys. 61 (2000) 7459–7465. https://doi.org/10.1103/PhysRevB.61.7459.

[71] M. Lazzeri, A. Vittadini, A. Selloni, Structure and energetics of stoichiometric TiO2 anatase surfaces, Phys. Rev. B - Condens. Matter Mater. Phys. 63 (2001) 155409. https://doi.org/10.1103/PhysRevB.63.155409.

[72] M. Ramamoorthy, D. Vanderbilt, R.D. King-Smith, First-principles calculations of the energetics of stoichiometric TiO2 surfaces, Phys. Rev. B. 49 (1994) 16721. https://doi.org/https://doi.org/10.1103/PhysRevB.49.16721.

[73] L. Mino, G. Spoto, A.M. Ferrari, CO2 capture by TiO2 anatase surfaces: A combined DFT and FTIR study, J. Phys. Chem. C. 118 (2014) 25016–25026. https://doi.org/10.1021/jp507443k.

[74] D.C. Sorescu, W.A. Al-Saidi, K.D. Jordan, CO2 adsorption on TiO2(101) anatase: A dispersion-

corrected density functional theory study, J. Chem. Phys. 135 (2011) 124701. https://doi.org/10.1063/1.3638181.

[75] F. Jiang, L. Yang, D. Zhou, G. He, J. Zhou, F. Wang, Z.G. Chen, First-principles atomistic Wulff constructions for an equilibrium rutile TiO 2 shape modeling, Appl. Surf. Sci. 436 (2018) 989–994. https://doi.org/10.1016/j.apsusc.2017.12.050.